

## RESEARCH ARTICLE

# Design Considerations of a New IPM Rotor With Efficient Utilization of PMs Enabled by Additive Manufacturing

AKBAR MOHAMMADI AJAMLOO<sup>1,2</sup>, MOHAMED N. IBRAHIM<sup>1,2,3</sup>, (Senior Member, IEEE), AND PETER SERGEANT<sup>1,2</sup>, (Senior Member, IEEE)

<sup>1</sup>Department of Electromechanical, Systems and Metal Engineering, Ghent University, 9052 Ghent, Belgium

<sup>2</sup>FlandersMake@UGent, Core Lab MIRO, 3001 Leuven, Belgium

<sup>3</sup>Electrical Engineering Department, Kafrelsheikh University, Kafr El Sheikh 33511, Egypt

Corresponding author: Akbar Mohammadi Ajamloo (Akbar.MohammadiAjamloo@ugent.be)



Funded by  
the European Union

This work was supported by the European Union under Marie Skłodowska Curie Doctoral-Industrial Project (HORIZON-MSCA-2021-DN-01) with the title “New Generation of Electrical Machines Enabled by Additive Manufacturing—EMByAM” and Research Foundation—Flanders (FWO) in the project entitled “Multi-Material Additive Manufacturing for Electrical Machines with increased performance (AM4EM)” under Grant S001721N.

**ABSTRACT** This paper presents a new design concept for interior permanent magnet (IPM) rotor using the capabilities of additive manufacturing (AM). In conventional laminated IPM topology, the presence of rotor ribs is essential for maintaining the mechanical integrity of the rotor. However, these pole ribs are a primary contributor to flux leakage, leading to inefficient utilization of costly rare-earth PMs. Addressing this challenge, a rib-less IPM rotor is proposed that takes advantage of the AM potential which eliminates the need for traditional ribs while maintaining the structural integrity of the rotor. Nevertheless, the additively manufactured cores, in contrast to conventionally laminated rotor cores, demand specific design considerations, especially in terms of eddy current loss and structural performance. In this regard, a strategy involving the incorporation of shallow grooves on the rotor surface is employed to mitigate eddy current loss. The mechanical performance of the proposed topology is carefully examined, and the impact of pole geometry on rotor displacement induced by centrifugal forces is investigated. To evaluate the performance of the proposed topology, an optimization procedure based on response surface methodology is conducted for both the proposed rotor and a conventional IPM rotor. The results indicate that the proposed IPM topology can offer significantly more efficient utilization of PMs and enhanced torque rating by approximately 8% compared to the laminated IPM topology.

**INDEX TERMS** 3D printing, additive manufacturing, eddy current loss, interior permanent magnet, IPM rotor, permanent magnet motor, response surface methodology, rib-less rotor, structural analysis.

## I. INTRODUCTION

Rare-earth Permanent Magnet (REPM) machines are now widely used in the automotive industry. Their superior characteristics such as higher torque density, efficiency and power factor make them preferable to other types of Electrical Machines (EMs) specifically, induction and synchronous reluctance machines (SynRMs) [1], [2]. Among REPM machines, interior PM (IPM) configuration has been widely

The associate editor coordinating the review of this manuscript and approving it for publication was Wuliang Yin<sup>1</sup>.

used owing to its enhanced mechanical stability and lower risk of PM demagnetization with respect to surface-mounted PM (SPM) topology [3]. However, the high price of RE materials and their undesirable environmental impact have raised serious concerns, thereby imposing limitations on their ongoing utilization. So, addressing these challenges is imperative for the sustainable and responsible integration of REPM machines in automotive applications.

Some studies have investigated the use of non-RE materials to replace the RE materials. However, these alternatives exhibit considerably lower torque density compared to REPM

machines, which is crucial for several industries, e.g. the automotive industry [4], [5]. In [6], a pole shaping strategy involving the utilization of rotor notches is introduced for RE-IPMs, where both the rotor notch and PM dimensions are adjusted in the axial direction. This approach led to an improvement of approximately 2.5% in PM utilization compared to the baseline, but with a significant increase in manufacturing complexity. Axially segmented rotor structures are proposed in [7] and subsequently investigated in [8], [9], [10], and [11], where the rotor comprises an IPM (or SPM) stack and a SynRM stack. These two stacks are mounted on the same shaft and displaced by a certain angle to align the PM and reluctance torque components. The findings indicate about 7% enhancement in torque and more efficient utilization of REPM. However, unbalanced axial force, mechanical complication due to the implementation of two different laminations, and the necessity for a non-magnetic separator between the IPM and SynRM stacks are the drawbacks of this topology. Asymmetric rotor structures are investigated in [12] and [13] to improve torque characteristics of REPMs by aligning the two torque components. It is reported that the total torque can be enhanced by up to 8% while keeping a fixed PM volume. Nevertheless, the topologies featuring an asymmetric design exhibit drawbacks such as high back-electromotive force (back-emf) harmonic distortion, increased core loss, and reduced efficiency at high rotational speeds [14].

Additive Manufacturing (AM) is an emerging topic in the context of EMs which is defined by American Society for Testing and Materials as “a process of joining materials to make parts from 3D model data, usually layer upon layer”. AM offers distinct advantages, including rapid prototyping, the potential for simplifying manufacturing processes, and reduced material usage when compared to conventional manufacturing methods [15], [16]. AM has been employed for all main components of EMs as illustrated in Fig. 1. Investigation into PMs using AM is still in its initial phases, with the printed PMs demonstrating a relatively lower energy density compared to the conventionally manufactured PMs [17]. In contrast, the fabrication of heat exchangers and windings using AM has reached a more advanced state and is well-suited for commercial applications [18], [19]. Soft magnetic cores produced through AM are currently in the development phase and have been applied to both stator and rotor cores of EMs. Currently, the application of AM to the stator is limited due to challenges associated with eddy current loss mitigation within the solid stator [20], [21]. In contrast, rotor core manufacturing using AM is more advanced owing to experiencing a quasi-DC magnetic field which induces tolerable -yet still considerable- eddy currents [22].

Superiority of the additively manufactured soft magnetic cores over the conventionally laminated cores can be regarded from two viewpoints. **1) Increasing the Silicon content to 6.5%:** It is well-known that increasing silicon content to around 6.5% in soft magnetic Fe-Si cores leads to higher

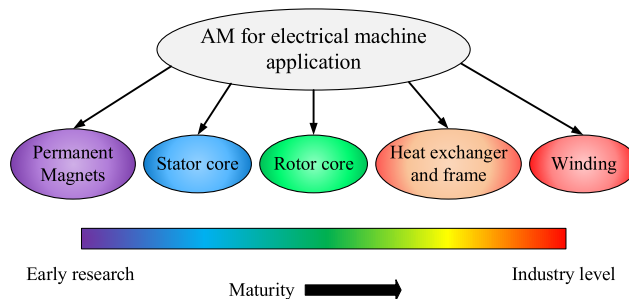


**FIGURE 1.** Application and current maturity index of additive manufacturing for various components of electrical machines.

magnetic permeability and lower eddy current losses, which is ideal for EMs. However, 6.5% silicon content in Fe-Si laminations is challenging to process by cold rolling due to its highly brittle feature. Consequently, the silicon content in conventional Fe-Si lamination used in EMs is kept around 3.5% [23]. On the contrary, metal AM avoids the high stress during printing, thereby enables manufacturing of Fe-6.5wt%Si cores with significantly enhanced permeability and resistivity as reported in [24] and [25]. Notably in [24], a Fe-6.7wt%Si core was successfully prototyped and achieved a maximum relative permeability of 31,000 and an electrical resistivity of  $82 \mu\Omega\cdot\text{cm}$ , surpassing the characteristics of conventional steel grades (i.e. 35A300 with a maximum permeability of 8,200 and a resistivity of  $51 \mu\Omega\cdot\text{cm}$ ). **2) More design flexibility:** The freedom in the geometrical design of conventionally laminated cores is primarily restricted to the 2D plane. In contrast, for additively manufactured cores, complex 3D configurations can be fabricated, allowing for more creative designs. In [26], an advanced EM with a conical air gap and 3D flux path was designed offering two-times power density compared to its baseline. In [27], a new line-start SynRM was designed with the axial length of the line-start core smaller than that of the SynRM core, resulting in a more compact structure. An additively manufactured stator for an axial flux PM machine was presented in [20] and [28] utilizing Fe-6.7wt%Si powder as its core material. A special Hilbert shape was adopted to limit the eddy current losses in the stator. The results indicated an approximately 4.5% improvement in torque density. Developments in rotor cores of EMs, reported in [29] and [30], involved shape optimization aimed at achieving enhanced torque density and reduced torque fluctuations.

In summary, the research on additively manufactured EMs is moving forward to improve performance of EMs. Despite notable progress, addressing eddy current loss in solid cores remains a significant challenge. Furthermore, previous studies on additively manufactured rotors of EMs lack structural analysis, particularly at high rotational speeds. In this regard, the contributions of this study are as follows: 1) Introducing a new rotor structure by leveraging the capabilities of AM to enhance torque density and achieve a more efficient utilization of REPMs. The proposed structure is not only efficient

but also features a straightforward manufacturing process. 2) Carrying out performance optimization and eddy current loss mitigation methodology for the solid rotor which is challenging in additively manufactured cores. 3) Conducting structural analysis on the new rotor concept enabled by AM and addressing design considerations aimed at optimizing its structural performance.

In this study, a new concept of rib-less IPM rotor relying on features of AM is proposed and compared to its conventional laminated counterpart. To achieve an optimum design, Response Surface Methodology (RSM) is used as the optimization technique to achieve the highest torque per PM volume with the desired torque ripple. Due to solid structure of the additively manufactured cores, an effective eddy current loss mitigation technique is adopted and investigated in details. To investigate the mechanical performance of the proposed topology, structural analysis is carried out, and corresponding design considerations are addressed. The proposed rotor structure and concept is discussed in section II. Then, the design optimization procedure based on RSM is carried out for both laminated and proposed IPM rotors in section III. Next, investigation on eddy current loss mitigation for the solid rotor is presented in section IV. In the final section, mechanical analysis of the proposed topology is presented.

## II. PROBLEM STATEMENT AND TOPOLOGY CONCEPT

Cross sectional view of the conventional IPM topology is depicted in Fig. 2(a) in which PMs' main and leakage flux paths are denoted by black and red lines, respectively. The main flux enters the air gap and contributes to torque production while the leakage flux closes its path via the pole ribs without any useful contribution. The flow of leakage flux continues until the pole ribs are fully saturated resulting in waste of REPMs volume. Notably, presence of the pole ribs is essential in laminated IPM rotors to maintain mechanical integrity of the rotor at the expense of the extra REPM volume. The integration of special support structures could potentially eliminate the need for pole ribs in the laminated IPM rotor. However, this approach may lead to increased rotor cost and complexity, coupled with a potential decrease in structural reliability, factors that might not sufficiently justify the elimination of pole ribs.

### A. ANALYSIS OF CONVENTIONAL IPM ROTOR VIA MAGNETIC EQUIVALENT CIRCUIT

Equivalent reluctance network of the conventional IPM machine is calculated and presented in Fig. 2(b), with the corresponding geometric parameters given in Fig. 3. In this regard PMs are modelled by an ideal current source ( $F_{pm}$ ) shunted by a leakage reluctance ( $R_{pm}$ ) as follows [31].

$$F_{pm} = B_r W_{pm} L_c, \quad R_{pm} = \frac{T_{pm}}{\mu_{pm} W_{pm} L_c} \quad (1)$$

where,  $L_c$ ,  $B_r$  and  $\mu_{pm}$  are the core axial length, remanent flux density and permeability of the PM, respectively. The

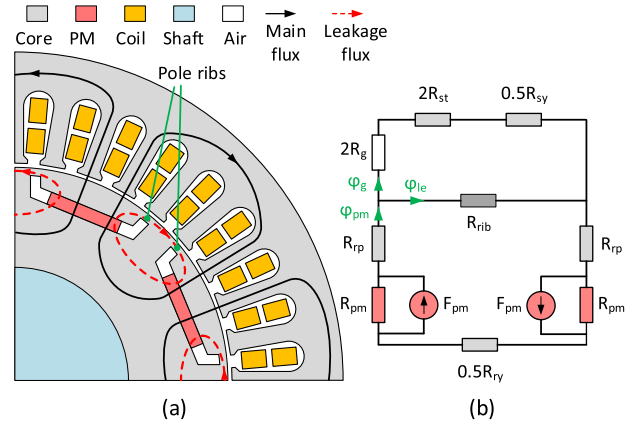


FIGURE 2. Conventional IPM machine. (a) Cross sectional view and flux paths. (b) Equivalent (net) reluctance network.

reluctances corresponding to rotor pole ( $R_{rp}$ ), rotor yoke ( $R_{ry}$ ), and stator teeth ( $R_{st}$ ) and yoke ( $R_{sy}$ ) are calculated as follows.

$$R_{rp} = \frac{T_{rp}}{\mu_{rp} W_{pole} L_c}, \quad R_{ry} = \frac{p T_{ry}}{\pi \mu_{ry} L_c (D_{ri} + T_{ry})} \quad (2)$$

$$R_{st} = \frac{\pi D_{si} H_{st}}{\mu_{st} N_s W_{pole} W_{st} L_c}, \quad R_{sy} = \frac{p T_{sy}}{\pi \mu_{sy} L_c (D_{so} - T_{sy})} \quad (3)$$

Here,  $p$  and  $N_s$  are the number of poles and stator teeth,  $\mu_{rp}$ ,  $\mu_{ry}$ ,  $\mu_{st}$ ,  $\mu_{sy}$  denote the iron permeabilities corresponding to the rotor pole, rotor yoke, stator teeth and stator yoke, respectively. Next, reluctances associated with air gap ( $R_g$ ) and rotor pole rib ( $R_{rib}$ ) can be written as follows.

$$R_g = \frac{L_g}{\mu_0 W_{pole} L_c}, \quad R_{rib} = \frac{W_r}{\mu_{rib} T_r L_c} \quad (4)$$

where,  $\mu_{st}$  and  $\mu_{sy}$  are the permeabilities of air and iron rib respectively. After that all reluctances are calculated, the flux per pole ( $\phi_{pm}$ ) generated by PMs can be determined as in (5).

$$\phi_{pm} = \frac{R_{pm} F_{pm}}{R_{rp} + R_{pm} + 0.5(R_{ry} + R')}$$

$$R' = R_{rib} \parallel (2R_g + 2R_{st} + 0.5R_{sy}) \quad (5)$$

According to Fig. 2,  $\phi_{pm}$  is split into the leakage flux ( $\phi_{le}$ ) and air gap flux ( $\phi_g$ ) where their ratio can be calculated by the following equation.

$$\phi_{pm} = \phi_{le} + \phi_g, \quad \frac{\phi_{le}}{\phi_g} = \frac{2R_g + 2R_{st} + 0.5R_{sy}}{R_{rib}} \quad (6)$$

Accordingly, the leakage and air gap flux components can be calculated as in (7) and (8), respectively.

$$\phi_{le} = \phi_{pm} \frac{1}{1 + R_{rib} / (2R_g + 2R_{st} + 0.5R_{sy})} \quad (7)$$

$$\phi_g = \phi_{pm} \frac{1}{1 + (2R_g + 2R_{st} + 0.5R_{sy}) / R_{rib}} \quad (8)$$

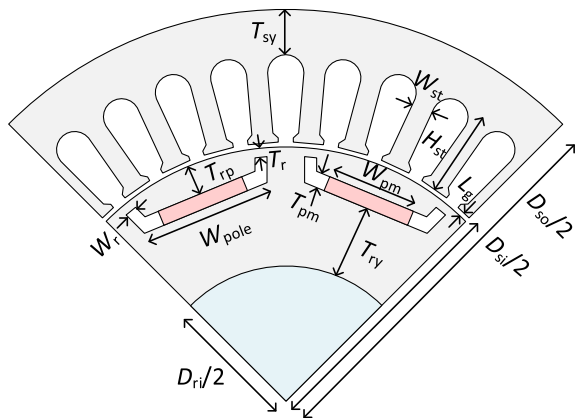


FIGURE 3. Geometric parameters of IPM topology.

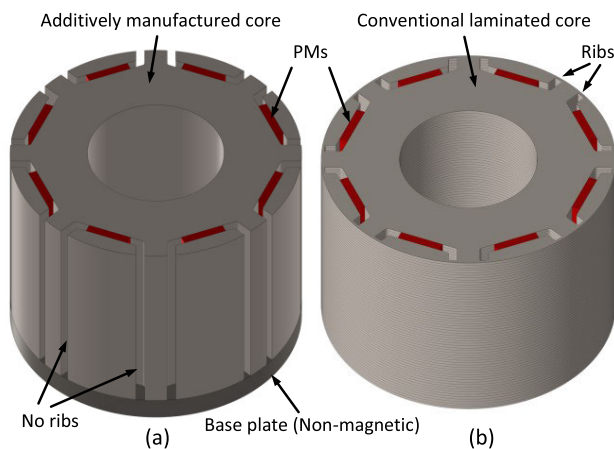


FIGURE 4. 3D view of the IPM rotor topologies. (a) Proposed rotor enabled by AM. (b) Conventional laminated rotor.

### B. PROPOSED IPM ROTOR ENABLED BY AM

In the previous part, a reluctance network for the laminated IPM rotor was developed and the corresponding reluctances were calculated. Then, the net flux per pole consisting of leakage and air gap components was determined. As it can be understood from (6), the ratio of leakage flux to air gap flux can be minimized by increasing the reluctance associated with the rotor pole ribs ( $R_{rib}$ ). This approach leads to the transfer of almost all the PM flux to the air gap, actively contributing to torque production and resulting in optimal utilization of the PM volume.

In order to minimize the PM leakage flux and achieve an efficient utilization of PMs, a rib-less IPM rotor structure is proposed and compared to the laminated topology in Fig. 4(a). The proposed rotor can be printed on a non-magnetic base plate which ensures mechanical integrity of the IPM rotor. After the part is printed, appropriate heat treatment should be carried out to relief stress and increase grain size of the soft magnetic core. This enhances both the mechanical and magnetic properties of the ferromagnetic

TABLE 1. Optimization variables of RSM.

Optimization variable	Symbol	Variation range	Optimal value
Rotor pole width (mm)	$W_{pole}$	[15 , 25]	16.5
Rotor pole depth (mm)	$T_{rp}$	[1 , 5]	3
PM width (mm)	$W_{pm}$	[4 , 14]	12
PM thickness (mm)	$T_{pm}$	[2 , 3.5]	2
Rib width (mm)	$W_r$	[1 , 2.5]	1.8

core [32]. Next, PMs are inserted into the rotor cavities and the shaft is installed in the rotor.

Apart from the benefits gained by eliminating the rotor ribs, employing Fe-6.7wt%Si powder for the 3D printing of the IPM rotor brings forth further advantages. Substantial enhancement in relative permeability, electrical resistivity and yield strength compared to the laminated structure are achieved as reported in [24] and [33]. Nevertheless, despite the increased electrical resistivity, eddy current loss in the printed rotor can be significantly higher than the laminated rotor caused by time and space harmonics. Moreover, mechanical performance of the proposed rib-less rotor needs to be evaluated carefully specially at high rotational speeds. These challenges are comprehensively addressed in this paper. In the next section, design and optimization procedure of both conventional and proposed IPM topologies is discussed.

### III. DESIGN AND OPTIMIZATION VIA RESPONSE SURFACE METHODOLOGY

To ensure a meaningful comparison between the proposed and conventional IPM topologies, it is crucial to conduct a thorough design and optimization process. This process initiates with the general sizing of the machine to deliver the rated power of 450 W at 750 rpm. Subsequently, the armature design is executed utilizing classical design equations [34]. This involves determining various armature parameters such as the stator outer diameter ( $D_{so}$ ), stator inner diameter ( $D_{si}$ ), number of stator teeth ( $N_s$ ), stator yoke thickness ( $T_{sy}$ ), stator tooth width ( $W_{st}$ ), and height ( $H_{st}$ ). The air gap length is ( $L_g$ ) set at 0.3 mm, ensuring a minimum safe clearance between the rotor and stator in the motor of this size. Moving to the rotor parameters, the pole width ( $W_{pole}$ ), pole depth ( $T_{rp}$ ), PM width ( $W_{pm}$ ) and thickness ( $T_{pm}$ ), and the width of the rotor pole cavity ( $W_r$ ) are identified as the primary rotor parameters and thus selected as optimization variables. Notably, the rotor yoke thickness ( $T_{ry}$ ) is excluded as an optimization variable since it is intentionally oversized in the optimization stage to maintain low magnetic flux density in that region. Therefore, five key rotor parameters are designated for optimization, as outlined in Table 1 and Fig. 3. The following objective function and constrains are used for the optimization procedure.

**TABLE 2.** Main specifications of the IPM topologies.

Parameter	Unit	Value
Rated Power	W	450
Rated Speed	rpm	750
Stator outer diameter	mm	131
Stator inner diameter	mm	86
Stack length	mm	50
Number of poles	-	8
Current density	A/mm <sup>2</sup>	5
Number of stator slots	-	36
Number of coil turns per phase	-	696
Air gap length	mm	0.3

- 1) Objective function: Maximum torque per PM volume.
- 2) Constraints:
  - 6 N.m < Nominal torque < 6.2 N.m
  - Torque ripple < 25% of the rated torque.
  - Armature parameters given in Table 2.
  - The optimization variables given in the next section.

#### A. OPTIMIZATION OF THE CONVENTIONAL IPM TOPOLOGY

Although there have been some analytical approaches towards modelling of EMs, Finite Element Analysis (FEA) is the most popular tool for precise modelling of complex geometries as well as non-linear behavior of iron core. However, high computational effort is a considerable factor associated with FEA, especially in FEA-based optimization problems. In this regard, RSM stands out as an efficient and yet reliable optimization approach, with a demonstrated track record in the field of EM design [35].

Central Composite Design (CCD) is used to generate the optimization sample points, which are presented in the form of an orthogonal array in Table 3. After performing the FEA simulations, the responses (average torque, torque per PM volume) corresponding to each sample point are extracted. Then, a quadratic regeneration model based on the least square method is established between responses and optimization variables as in (9).

$$Y = a_0 + \sum_{i=1}^n a_i x_i + \sum_{i=1}^n b_i x_i^2 + \sum_{i=1}^{n-1} \sum_{j=i+1}^n c_{i,j} x_i x_j \quad (9)$$

Here,  $Y$ ,  $x_i$  and  $n$  are optimization response,  $i^{\text{th}}$  optimization variable and number of variables respectively. The coefficients  $a_0$ ,  $a_i$ ,  $b_i$  and  $c_{i,j}$  correspond to the average, linear, quadratic, and interaction terms, respectively.

The precision of the regression model is assessed by the coefficient of determination, denoted as  $R^2$ , defined

**TABLE 3.** RSM's required samples.

Sample No.	Optimization variables (mm)				
	$W_{pole}$	$T_{rp}$	$W_{pm}$	$T_{pm}$	$W_r$
1	15	1	4	2	2.5
2	25	1	4	2	1
3	15	5	4	2	1
4	25	5	4	2	2.5
5	15	1	14	2	1
6	25	1	14	2	2.5
7	15	5	14	2	2.5
8	25	5	14	2	1
9	15	1	4	3.5	1
10	25	1	4	3.5	2.5
11	15	5	4	3.5	2.5
12	25	5	4	3.5	1
13	15	1	14	3.5	2.5
14	25	1	14	3.5	1
15	15	5	14	3.5	1
16	25	5	14	3.5	2.5
17	15	3	9	2.75	1.75
18	25	3	9	2.75	1.75
19	20	1	9	2.75	1.75
20	20	5	9	2.75	1.75
21	20	3	4	2.75	1.75
22	20	3	14	2.75	1.75
23	20	3	9	2	1.75
24	20	3	9	3.5	1.75
25	20	3	9	2.75	1
26	20	3	9	2.75	2.5
27	20	3	9	2.75	1.75

as follows.

$$R^2 = 1 - \frac{SS_E}{SS_T} \quad (10)$$

where,  $SS_T$  is the total sum of squares, and  $SS_E$  represents the sum of squares of the error, respectively [36].  $R^2$  value closer to unity indicates a model with higher accuracy.

According to the aforementioned discussion, regression models corresponding to the average torque ( $T_{ave}$ ) and torque per PM volume are determined, with  $R^2$  value for both responses being approximately 0.98. This indicates a very high accuracy of the fitted models. Therefore, meeting the objective function and adhering to constraints is accomplished by selecting the optimal values for the variables as specified in Table 1. The influence of pole width ( $W_{pole}$ ) and PM width ( $W_{pm}$ ) on average torque, torque ripple and torque per PM volume is illustrated in Fig. 5(a)-(c), respectively, with the remaining variables fixed at their optimum values. It is observed that the main factor influencing average torque and torque per PM volume is associated more with the PM width ( $W_{pm}$ ) rather than the pole width ( $W_{pole}$ ). Conversely, torque ripple is mainly affected by  $W_{pole}$  rather than  $W_{pm}$ , with the optimal choices for  $W_{pole}$  being 16.5 mm, 20 mm, or 24.5 mm, resulting in the minimum torque ripple.

#### B. OPTIMIZATION OF THE PROPOSED RIB-LESS IPM TOPOLOGY

So far, design and optimization of the conventional IPM topology has been discussed. To ensure a fair comparison,

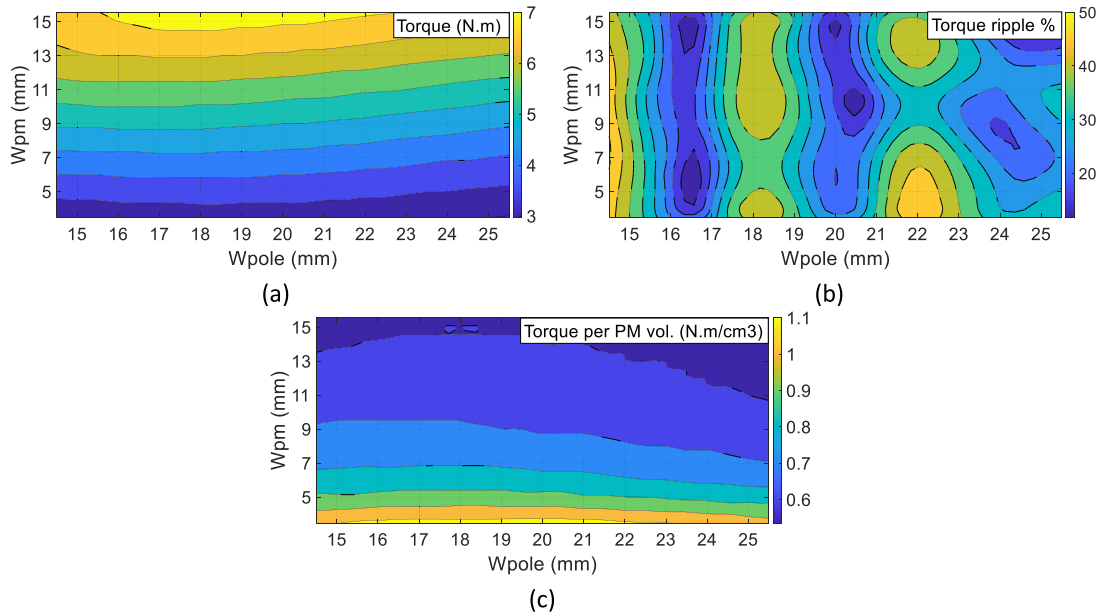


FIGURE 5. Variation of optimization responses with  $W_{pole}$  and  $W_{pm}$ . (a) Torque. (b) Torque ripple. (c) Torque per PM volume.

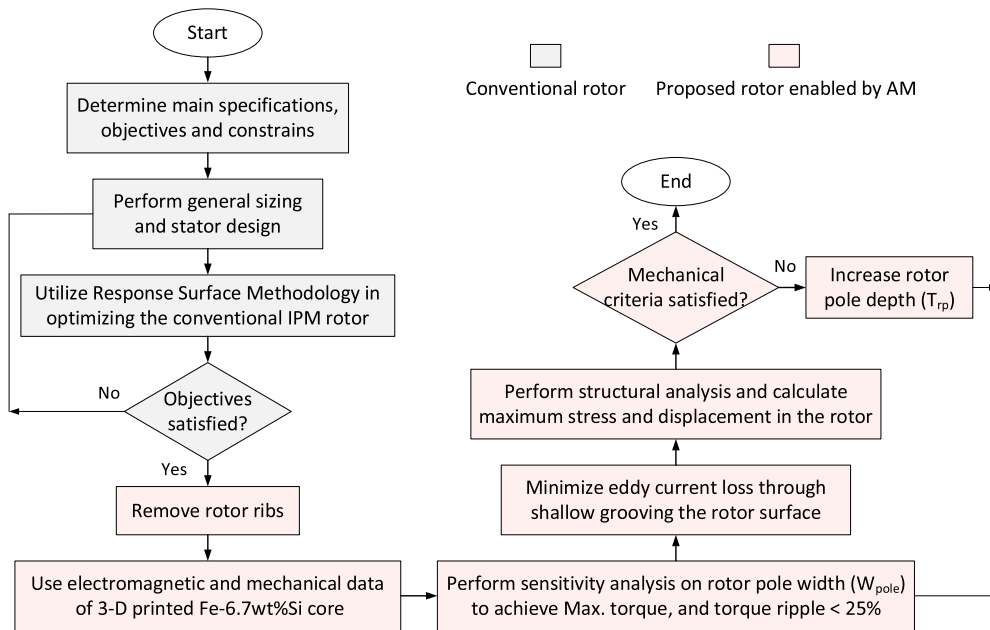


FIGURE 6. Proposed algorithm for design and optimization of the conventional rotor and the rib-less rotor enabled by AM.

the proposed topology incorporates identical PM dimensions and adheres to the parameters outlined in Table 2. The only changes made involve the modification of the rotor pole geometry through a new round of optimization, along with a change in the rotor core material to Fe-wt6.7%Si. Figure 6 displays  $B-H$  and  $\mu-H$  curves of the proposed IPM rotor (printed Fe-6.7wt%Si), highlighted in red. The curves are then compared with those of the conventional laminated

topology (lamination grade: 35A300), showcased in black. Accordingly, the utilization of 6.7% silicon contributes to achieving the highest permeability of 31,000 A/m and electrical resistivity of  $82 \mu\Omega\cdot\text{cm}$  for 3D printed cores. This is accompanied by a reduction in saturation flux density, as expected due to the increased silicon content.

The proposed design and optimization algorithm for the under-study IPM topologies is presented in Fig. 7. The steps

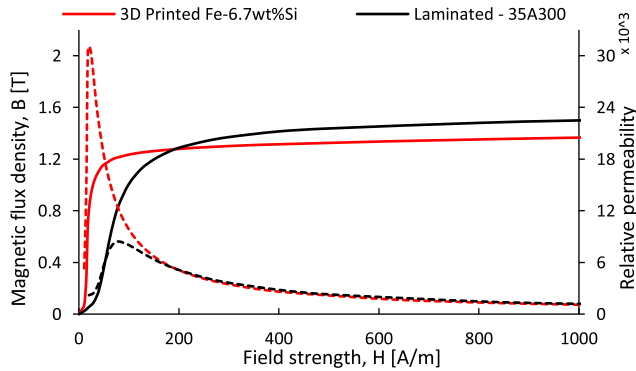


FIGURE 7. B-H curve and permeability (dashed line) data of the 3-Printed Fe-6.7wt%Si reported in [24] vs conventional 35A300 lamination.

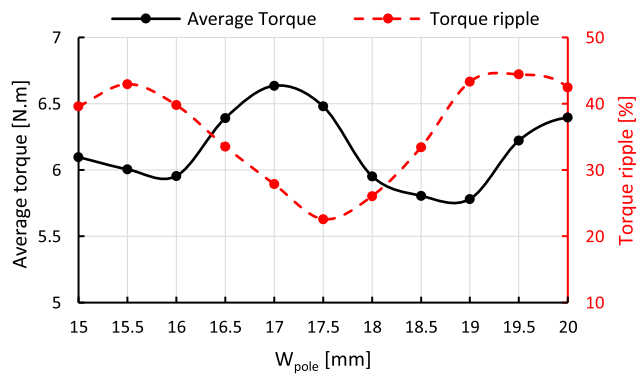


FIGURE 8. Sensitivity of the average torque and torque ripple of the proposed rib-less rotor to  $W_{pole}$ .

related to each topology are distinguished by different colors. Accordingly, after completing optimization steps for the conventional IPM topology, the optimization steps corresponding to the proposed rib-less rotor are initiated. In this regard, rotor ribs are removed from the previously optimized rotor. Subsequently, the electromagnetic and structural characteristics of the printed Fe-6.7wt%Si sample core are used for the rib-less rotor. Since torque ripple is highly sensitive to the rotor geometry, removal of the ribs results in an increased torque ripple. Consequently, a sensitivity analysis is essential to attain a tolerable torque ripple. In this regard, a sensitivity analysis is conducted to determine a new optimal value for pole width ( $W_{pole}$ ) and pole depth ( $T_{rp}$ ) while maintaining other parameters fixed, including dimensions of the PMs. The optimal value for  $W_{pole}$  is determined according to electromagnetic requirements, whereas the optimal value for  $T_{rp}$  is determined based on structural considerations, which will be elaborated in Section V. Accordingly, the average torque and torque ripple are calculated with respect to  $W_{pole}$  for the rib-less IPM machine, and the results are depicted in Fig. 8. As evident from the results, there is a notable variation in torque ripple at different values of  $W_{pole}$ , with the minimum value being 23% observed at  $W_{pole} = 17.5$  mm. Afterwards, special measures should be adopted for eddy current loss

reduction in the rib-less rotor, followed by structural analysis which will be presented in the upcoming sections.

#### IV. ROTOR EDDY CURRENT LOSS MINIMIZATION

The issue of eddy current loss in 3D printed cores exposed to AC magnetic field is a major concern even with high electrical resistance achieved by increased silicon content. Several studies have addressed the mitigation of eddy current loss in 3D printed cores by incorporating especial geometric patterns. However, the case studies focused on simple toroid with wound primary and secondary windings [37], [38]. The limitation of these studies is evident in the fact that the majority of the investigated geometric shapes are applicable only to toroid cores, rather than EM cores. Consequently, the potential for 3D printing in stator cores which are exposed to high-amplitude AC magnetic field is currently limited due to excessive eddy current losses. On the contrary, eddy current loss in the rotor of IPM synchronous machines which experiences a quasi-DC magnetic field, is relatively low. Nevertheless, this can still lead to temperatures rise beyond the allowed limit for REPMs, resulting in irreversible demagnetization [39]. In this context, the mitigation of eddy current losses for IPM rotor is addressed here to cover the insufficiency of practical solution for this issue.

According to Bertotti loss theory in [40], iron loss in a magnetic core is divided into hysteresis loss ( $P_{hys}$ ), classical eddy current loss ( $P_{cl}$ ), and excess loss ( $P_{ex}$ ) as in (11).

$$P_{iron} = K_{hys}fB_m^2 + K_{cl}f^2B_m^2 + K_{exc}f^{1.5}B_m^{1.5} \quad (11)$$

where,  $K_{hys}$  is the hysteresis loss coefficient,  $B_m$  is the amplitude of magnetic flux density, and  $K_{cl}$  and  $K_{exc}$  denote the coefficients corresponding to classical eddy current loss and excess loss, respectively.

In the rotor of a synchronous machine, iron losses arise from high-frequency magnetic field components, commonly referred to as time and space harmonics. While hysteresis and excess losses are solely influenced by the micro-structure properties of the core, classical eddy current loss is also dependent on the core's geometry. In this regard, the coefficient  $K_{cl}$  is notably higher for a solid core compared to a laminated core. Consequently, in a printed IPM rotor with a solid structure, the predominant contributor to the majority of iron losses is the classical eddy current loss.

In the context of electromagnetic field theory, the amplitude of a magnetic field that penetrates a conductive material diminishes to approximately 37% of its surface value at a specific depth known as the skin depth ( $\delta$ ). This skin depth is influenced by the frequency of the magnetic field ( $f_m$ ), the electrical resistivity ( $\rho_c$ ), and the relative permeability ( $\mu_c$ ) of the core [41].

$$\delta = \sqrt{\frac{\rho_c}{\pi \mu_0 \mu_c f_m}} \quad (12)$$

So, the eddy currents induced by high-frequency magnetic field tend to concentrate on the surface of the solid rotor, a phenomenon known as the skin effect.

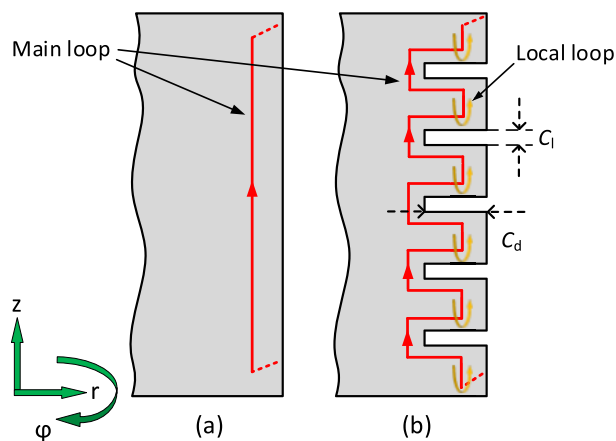


**FIGURE 9.** Cross-sectional views of eddy current path (schematic) in (a) non-grooved core, and (b) shallow grooved core. Note that the grooves are in z-direction, i.e. they are circular grooves at several positions along the axis of the machine.

In this regard, a technique based on shallow grooving the rotor surface is proposed here as an effective solution to mitigate eddy current loss. Fig. 9 represents cross-sectional views of grooved and non-grooved rotors with their respective eddy current paths. Accordingly, the eddy current follows a straight path along the axial direction in a non-grooved rotor. Utilizing shallow grooves serves as a barrier, causing a deviation in the path of eddy current flow. This leads to an elongated path and increased resistance, consequently reducing the induced eddy currents.

To mitigate eddy current losses in the proposed rib-less IPM rotor, a finite number of shallow grooves (denoted as  $N_g$ ) has been introduced, each characterized by specific length ( $C_l$ ) and depth ( $C_d$ ), as depicted in Figure 9 (b). The choice of the minimum groove length, set at 0.2 mm, aligns with practical considerations related to the 3D printing of ferromagnetic cores [21]. The optimization of two variables—namely the number of grooves and their depth—is essential for achieving the minimum rotor eddy current loss. To systematically address this optimization, a comprehensive parametric study has been conducted using 3D FEA, wherein the eddy current loss in the rotor is meticulously calculated. To ensure accurate computations without an excessive computational burden, a skin depth-based mesh has been implemented in Ansys Maxwell. The rotor’s eddy current loss is calculated at the rated speed of 750 rpm under full load condition, investigating various numbers of axial grooves ( $N_g$ ) ranging from 0 (representing a non-grooved rotor) to 20. Additionally, groove depths ( $C_d$ ) ranging from 0.5 mm to 2 mm are examined for each  $N_g$ . The obtained loss data is normalized based on the eddy current loss of the non-grooved rotor, and the findings are illustrated in Fig. 10. This figure presents a graphical representation of the variation in eddy current loss across different depths and numbers of shallow grooves in the rib-less IPM rotor. This visualization allows for a clear understanding of the impact of groove parameters on

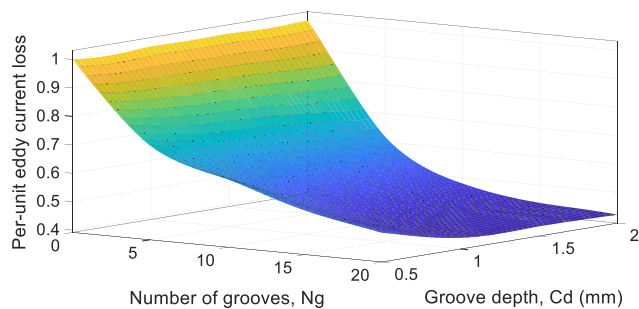


**FIGURE 10.** Effect of number of grooves and groove depth on the eddy current loss for the rib-less IPM rotor.

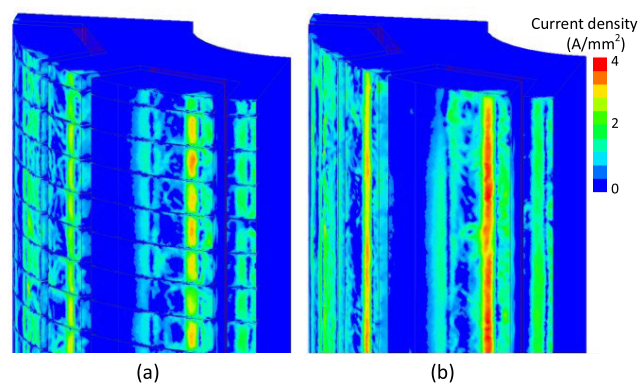


**FIGURE 11.** Contour plot of eddy current in the rib-less IPM rotor, (a) with optimal shallow grooves and (b) without grooves.

mitigating eddy current losses, aiding in the optimal design of the rotor for improved performance. Accordingly, there can be seen a noticeable inverse correlation between eddy current loss and the number of grooves. This inverse relationship suggests that the impact of extra grooves on eddy current loss decreases as the number of grooves increases. The impact of groove depth on eddy current loss is less prominent than the effect of the number of grooves. Deeper grooves lead to a decrease in eddy current loss. However, the effect of additional groove depth diminishes as the grooves become deeper, a trend similar to the observed pattern with the number of grooves. According to the analysis, the rib-less IPM rotor is configured with 10 grooves, each having a depth of 1.5 mm, as depicted in Fig. 11, illustrating the distribution of eddy current density. A noticeable reduction in surface eddy current is observed in the grooved rotor compared to its non-grooved counterpart. As a result, the eddy current loss in the rotor decreases from 5 W to approximately 2.2 W after the implementation of shallow grooving, indicating a significant reduction of more than 50% in the eddy current loss.

To gain a more comprehensive understanding of the effectiveness of the proposed method, the rotor eddy current losses for the solid rotor (non-grooved) and the rotor with optimal shallow grooves are calculated, under open circuit and full-load conditions. These calculations are done for a wide range of rotational speeds, extending up to four times the rated

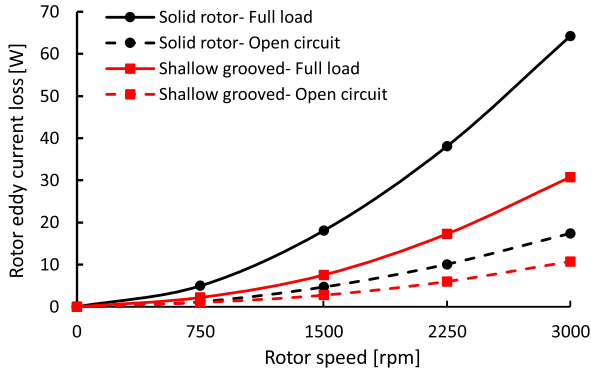


FIGURE 12. Rotor eddy current loss in the solid rotor and the rotor with optimal shallow grooves at open circuit and full-load conditions.

speed of 750 rpm and presented in the Fig. 12. In open-circuit conditions, eddy current losses in the rotor is induced by the slotting effect caused by the stator slot openings, while under full-load conditions, the eddy current losses stem from both the slotting effect and the high-frequency magnetic field components generated by the armature current. The investigation reveals that the proposed shallow grooving technique substantially reduces eddy current losses in the rotor, both at no-load and full-load conditions, across a wide range of operating speeds.

V. STRUCTURAL ANALYSIS AND PERFORMANCE COMPARISON

In this section mechanical performance of the proposed rotor topology is addressed to evaluate its structural integrity. This is an important consideration associated with design of the rib-less rotor, particularly at rotational speeds above its rated speed. Next, overall performance of the proposed IPM rotor is discussed and compared to the conventional topology.

A. STRUCTURAL ANALYSIS

According to the algorithm presented in Fig. 7, the structural analysis is to be conducted as the final stage in the design and optimization process of the proposed rotor enabled by AM. The mechanical properties of the rotor core are derived from measurements conducted on 3D printed Fe-6wt%Si samples in [33] and listed in Table 4. Accordingly, enhanced mechanical properties are noticed for additively manufactured Fe-Si core compared to conventional Fe-Si laminations. For the base plate, stainless steel AISI 316 is chosen due to its non-magnetic properties and desirable mechanical characteristics. The analysis is carried out at a rotational speed of 4500 rpm, which is six times its rated speed. In this regard, von Mises stress distribution in the proposed IPM rotor is calculated and illustrated in Fig. 13. Notably, the highest stress is observed at the base of the rotor cavities. The maximum stress recorded is approximately 150 MPa, significantly below the yield strength of the core materials, indicating a mechanically safe performance.

TABLE 4. Mechanical properties of materials [33], [42], [43].

Material	Yield strength (MPa)	Tensile strength (MPa)	Young's modulus (GPa)	Poisson ratio
Printed Fe-6wt%Si	631	685	190	~0.3
35A300 lamination	393	523	210	
AISI 316	483	656	200	

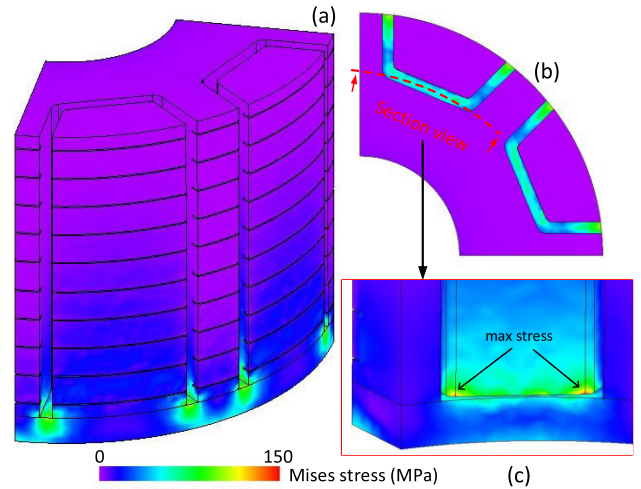


FIGURE 13. Von Mises stress distribution in the rib-less IPM rotor at 4500 rpm. (a) Isometric view. (b) Top view. (c) Section view.

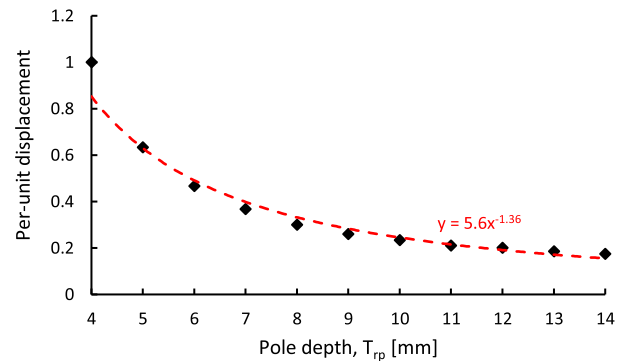


FIGURE 14. Per-unit value of maximum displacement in the rotor versus rotor pole depth.

In addition to stress analysis, the maximum displacement serves as another criterion for ensuring the mechanical safety of motor operation. Excessive displacement poses a risk of contact between the rotor and stator, potentially leading to mechanical failure. Given that the rotor poles are supported only from the bottom side, the highest displacement occurs at the top side. Consequently, certain measures should be adopted to limit the maximum displacement. The analysis indicate that the rotor displacement is predominantly affected by rotor pole depth ( $T_{rp}$ ). To have a better insight, maximum

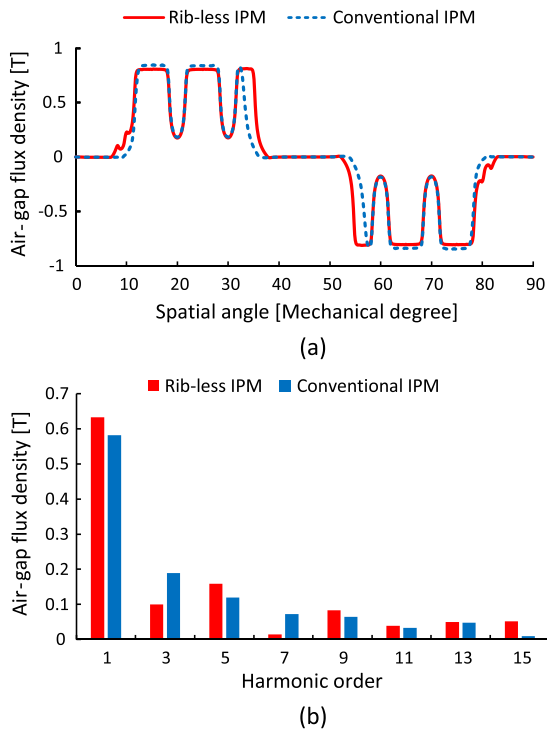


FIGURE 15. Comparison of open-circuit flux density in middle of air gap. (a) Waveforms. (b) Harmonic components.

displacement versus  $T_{rp}$  is calculated and presented in Fig. 14. As it can be noticed, there is a noticeable inverse correlation between maximum displacement and  $T_{rp}$ . As mentioned earlier in Section III, the rotor pole depth for the rib-less rotor is set at 10 mm. This choice signifies a decrease in displacement by more than 75% with respect to the scenario where  $T_{rp}$  is set at 4 mm.

**B. PERFORMANCE COMPARISON AND DISCUSSION**

Up to this point, design and optimization of both conventional and proposed rib-less IPM topologies have been conducted. Then, eddy current loss mitigation and structural analysis have been carried out for the rib-less IPM. In this part, performance of both topologies is investigated and compared.

To have a clear insight into the performance of the two IPM topologies, it is necessary to evaluate the distribution of magnetic flux density in the air gap. Consequently, air gap flux density distribution along with its spectra is calculated in open-circuit condition and illustrated in Fig. 15. Notably, fundamental component of air gap flux density in the rib-less IPM is higher than its conventional counterpart by approximately 9%. This difference is attributed to the removal of rotor ribs which serve as the main source of leakage flux in IPM rotor topologies as illustrated in Fig. 16. As it can be seen, rotor ribs of the conventional IPM rotor are heavily saturated, contributing to a deteriorated performance. In absence of rotor ribs, leakage flux in the rotor is minimized, leading to higher torque generation and a more efficient

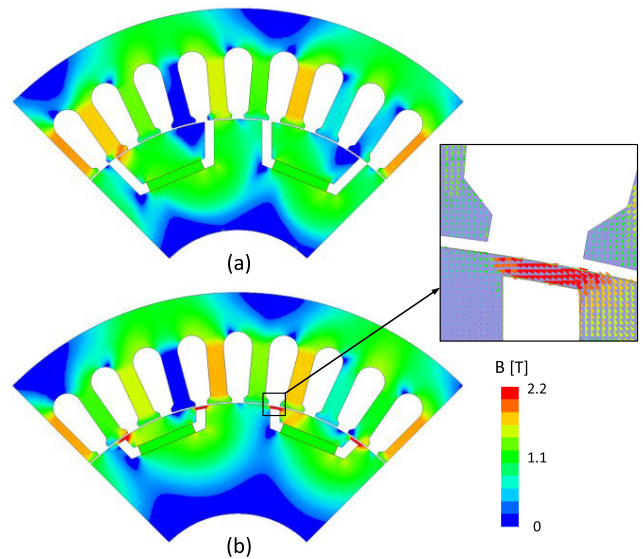


FIGURE 16. Magnetic flux density distribution in IPM topologies. (a) Rib-less IPM. (b) Conventional IPM.

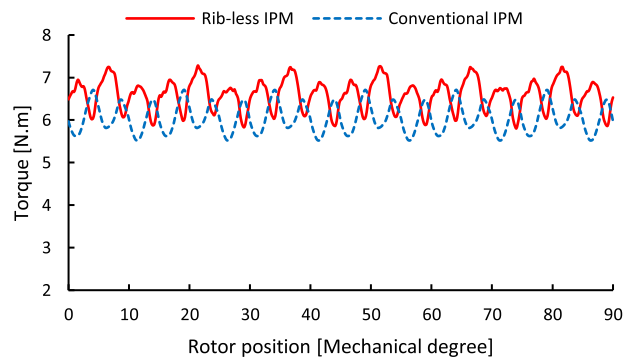


FIGURE 17. Average torque versus current angle at rated load.

utilization of PMs. To gain a better understanding of the differences in torque performance between the two topologies, the torque-versus-current-angle is calculated at the rated armature current and depicted in Fig. 17. Accordingly, a superior torque characteristic is noticed for the proposed rib-less IPM with respect to the conventional topology. Instantaneous torque profile of the IPM topologies at rated load are calculated and presented in Fig. 18. The rib-less IPM exhibits an approximately 8% higher average torque compared to the conventional IPM.

The overall performance of the proposed rib-less IPM topology is compared to its conventional counterpart and presented in Table 5. For a fair basis for comparison, both topologies were optimized based on the discussion presented in Section III, utilizing the same armature parameters and PM dimensions. In this regard, it is revealed that the proposed topology exhibits enhanced torque capability and more efficient utilization of rare-earth PMs by approximately 8%. The proposed topology demonstrates an enhanced output power, yielding approximately 520 W, compared to the conventional

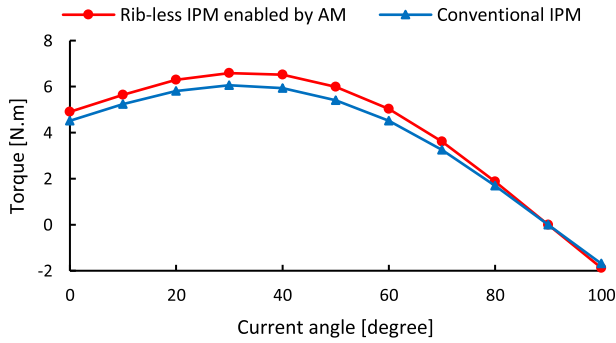


FIGURE 18. Instantaneous torque profile of the rib-less and conventional IPM topologies.

TABLE 5. Overall performance of the IPM topologies.

Item	Conventional IPM	Rib-less IPM
Torque (N.m)	6.1	6.6
Output power (W)	479.1	518.4
Torque/PM vol. (N.m/cm <sup>3</sup> )	0.64	0.69
Torque ripple (%)	19	23
Peak cogging torque (N.m)	0.18	0.25
Rotor eddy current loss (W)- 3D FEA	1.2	2.2
Stator core loss (W)	24.9	25.1
Efficiency (%)	83.3	84.2
Rated Speed (rpm)	750	
Copper loss (W)	70	
PM volume (cm <sup>3</sup> )	9.6	

IPM, which achieves roughly 480 W, all while maintaining fixed copper loss and PM volume. Additionally, the proposed IPM exhibits a commendable efficiency of 84.2%, surpassing the conventional counterpart, which attains an efficiency of 83.3%. Nevertheless, despite the efforts made to reduce rotor eddy current loss by introducing shallow grooves, the loss remains higher than the conventional IPM topology. The proposed topology exhibits inferior performance in terms of torque ripple and cogging torque compared to its traditional counterpart, leading to slightly higher levels of noise and vibration. Specifically, the torque ripple and peak cogging torque for the proposed topology are 23% and 0.25 N.m, respectively, while these values stand at 19% and 0.18 N.m for the conventional machine. This means that the proposed topology shows about 18% and 28% higher torque ripple and peak cogging torque respectively.

Consequently, this implies that the proposed topology is likely to experience higher vibration and noise levels under both no-load and full-load conditions in comparison to the conventional machine. Nevertheless, those values can be improved by skewing the rotor during the printing process but this is not considered in the current study.

TABLE 6. Cost comparison between the IPM rotors.

	Conventional rotor		Proposed rotor	
	Mass (kg)	Cost (USD)	Mass (kg)	Cost (USD)
35A300 lamination (including material waste)	3.1	4.0	-	-
Fe-6.7wt%Si powder (near-zero waste)	-	-	1.3	1.6
NdFeB magnet	0.071	6.0	0.065	5.5
Base plate (AISI 316)	-	-	0.15	0.2

In evaluating the cost implications, a comparative analysis conducted between the proposed rib-less IPM rotor and the conventional rotor. PM dimensions of both configurations are adjusted to yield the same rated power of 450 W at 750 rpm. The findings, detailed in Table 6, reveal a noteworthy difference in core material usage. The conventional rotor utilizes approximately 2.4 times more core material compared to the proposed rotor. This discrepancy arises from the efficiency of additive manufacturing, where minimal powder material is wasted, contrasting with the substantial material waste in the production of the conventional rotor. Consequently, the additively manufactured rotor core demonstrates significantly lower material usage compared to its laminated counterpart. Another cost-efficient aspect of the proposed IPM rotor lies in its higher torque per PM volume characteristic, leading to reduced usage of expensive rare-earth PMs with respect to the conventional topology. This contributes to sustainability requirements in design and manufacturing of high power density rare-earth PM machines.

## VI. CONCLUSION

In this study, a new rib-less IPM rotor configuration is proposed, utilizing the capabilities of additive manufacturing to enhance torque density and achieve a more efficient utilization of PMs. Furthermore, this paper addresses design considerations associated with electrical machines fabricated through additive manufacturing methods. The approach involves the application of shallow grooves to suppress eddy currents in the rotor. Through optimization of the number and depth of these grooves, a remarkable reduction in eddy current loss by more than 50% is achieved. Structural analysis is carried out, examining the influence of pole geometry on the mechanical performance of the rib-less IPM. The results reveal a significant decrease in rotor displacement - caused by centrifugal forces- by increasing the pole depth. To evaluate the performance of the proposed IPM enabled by AM, a comparison is made with the conventionally laminated IPM rotor. In this regard, both topologies underwent the same design and optimization procedure using response surface methodology, while keeping the armature parameters, rotor diameter, and PM dimensions fixed. The findings suggest that the proposed topology demonstrates a notable improvement,

offering a higher average torque and more efficient utilization of PMs by around 8% compared to the conventional topology. Although there is a slight increase in torque ripple from 19% in the conventional IPM machine to 23% in the proposed IPM machine, this remains within an acceptable limit. Nevertheless, conventional torque ripple reduction techniques could be applied to reduce the torque ripple.

## REFERENCES

- [1] S.-B. Jun, C.-H. Kim, J. H. Lee, J.-K. Kang, Y.-J. Kim, and S.-Y. Jung, "Parameter optimization for reducing torque ripple and harmonic losses of multi-layered interior permanent-magnet synchronous motors," *IEEE Access*, vol. 10, pp. 10536–10552, 2022.
- [2] C. Zhou, X. Huang, Z. Li, and W. Cao, "Design consideration of fractional slot concentrated winding interior permanent magnet synchronous motor for EV and HEV applications," *IEEE Access*, vol. 9, pp. 64116–64126, 2021.
- [3] Y. Xiao, Z. Q. Zhu, G. W. Jewell, J. T. Chen, D. Wu, and L. M. Gong, "Influence of armature reaction on magnetic-field-shifting effect in asymmetric interior permanent magnet machines," *IEEE Trans. Energy Convers.*, vol. 37, no. 2, pp. 1475–1488, Jun. 2022.
- [4] H. Cai, B. Guan, and L. Xu, "Low-cost ferrite PM-assisted synchronous reluctance machine for electric vehicles," *IEEE Trans. Ind. Electron.*, vol. 61, no. 10, pp. 5741–5748, Oct. 2014.
- [5] H. Tahanian, M. Aliahmadi, and J. Faiz, "Ferrite permanent magnets in electrical machines: Opportunities and challenges of a non-rare-Earth alternative," *IEEE Trans. Magn.*, vol. 56, no. 3, pp. 1–20, Mar. 2020.
- [6] Z. S. Du and T. A. Lipo, "Efficient utilization of rare Earth permanent-magnet materials and torque ripple reduction in interior permanent-magnet machines," *IEEE Trans. Ind. Appl.*, vol. 53, no. 4, pp. 3485–3495, Jul. 2017.
- [7] W. Zhao, F. Xing, X. Wang, T. A. Lipo, and B.-I. Kwon, "Design and analysis of a novel PM-assisted synchronous reluctance machine with axially integrated magnets by the finite-element method," *IEEE Trans. Magn.*, vol. 53, no. 6, pp. 1–4, Jun. 2017.
- [8] W. Zhao, H. Shen, T. A. Lipo, and X. Wang, "A new hybrid permanent magnet synchronous reluctance machine with axially sandwiched magnets for performance improvement," *IEEE Trans. Energy Convers.*, vol. 33, no. 4, pp. 2018–2029, Dec. 2018.
- [9] Z. Liu, Y. Hu, J. Wu, B. Zhang, and G. Feng, "A novel modular permanent magnet-assisted synchronous reluctance motor," *IEEE Access*, vol. 9, pp. 19947–19959, 2021.
- [10] A. Nobahari, A. Vahedi, and R. Nasiri-Zarandi, "A modified permanent magnet-assisted synchronous reluctance motor design for torque characteristics improvement," *IEEE Trans. Energy Convers.*, vol. 37, no. 2, pp. 989–998, Jun. 2022.
- [11] J.-X. Shen, Y.-Q. Lin, Y. Sun, X.-F. Qin, W.-J. Wan, and S. Cai, "Permanent magnet synchronous reluctance machines with axially combined rotor structure," *IEEE Trans. Magn.*, vol. 58, no. 2, pp. 1–10, Feb. 2022.
- [12] Y. Xiao, Z. Q. Zhu, G. W. Jewell, J. T. Chen, D. Wu, and L. M. Gong, "A novel asymmetric interior permanent magnet synchronous machine," *IEEE Trans. Ind. Appl.*, vol. 58, no. 3, pp. 3370–3382, May 2022.
- [13] Y. Xiao, Z. Q. Zhu, G. W. Jewell, J. Chen, D. Wu, and L. Gong, "A novel asymmetric rotor interior permanent magnet machine with hybrid-layer permanent magnets," *IEEE Trans. Ind. Appl.*, vol. 57, no. 6, pp. 5993–6006, Nov. 2021.
- [14] Y. Xiao, Z. Q. Zhu, S. S. Wang, G. W. Jewell, J. T. Chen, D. Wu, and L. M. Gong, "A novel asymmetric interior permanent magnet machine for electric vehicles," *IEEE Trans. Energy Convers.*, vol. 36, no. 3, pp. 2404–2415, Sep. 2021.
- [15] P. S. Ghahfarokhi, A. Podgornovs, A. Kallaste, A. J. M. Cardoso, A. Belahcen, T. Vaimann, H. Tiismus, and B. Asad, "Opportunities and challenges of utilizing additive manufacturing approaches in thermal management of electrical machines," *IEEE Access*, vol. 9, pp. 36368–36381, 2021.
- [16] A. Selema, M. N. Ibrahim, and P. Sergeant, "Metal additive manufacturing for electrical machines: Technology review and latest advancements," *Energies*, vol. 15, no. 3, p. 1076, Jan. 2022.
- [17] H. Wang, T. N. Lamichhane, and M. P. Paranthaman, "Review of additive manufacturing of permanent magnets for electrical machines: A prospective on wind turbine," *Mater. Today Phys.*, vol. 24, May 2022, Art. no. 100675.
- [18] H. Tiismus, A. Kallaste, T. Vaimann, and A. Rassõlkin, "State of the art of additively manufactured electromagnetic materials for topology optimized electrical machines," *Additive Manuf.*, vol. 55, Jul. 2022, Art. no. 102778.
- [19] A. Selema, M. N. Ibrahim, and P. Sergeant, "Additively manufactured ultralight shaped-profile windings for HF electrical machines and weight-sensitive applications," *IEEE Trans. Transport. Electrific.*, vol. 8, no. 4, pp. 4313–4324, Dec. 2022.
- [20] F. Nishanth, A. D. Goodall, I. Todd, and E. L. Severson, "Characterization of an axial flux machine with an additively manufactured stator," *IEEE Trans. Energy Convers.*, vol. 38, no. 4, pp. 2717–2729, Dec. 2023.
- [21] H. Tiismus, A. Kallaste, M. U. Naseer, T. Vaimann, and A. Rassõlkin, "Design and performance of laser additively manufactured core induction motor," *IEEE Access*, vol. 10, pp. 50137–50152, 2022.
- [22] L. Gargalis, V. Madonna, P. Giangrande, R. Rocca, M. Hardy, I. Ashcroft, M. Galea, and R. Hague, "Additive manufacturing and testing of a soft magnetic rotor for a switched reluctance motor," *IEEE Access*, vol. 8, pp. 206982–206991, 2020.
- [23] F. Fiorillo, G. Bertotti, C. Appino, and M. Pasquale, "Soft magnetic materials," in *Wiley Encyclopedia of Electrical and Electronics Engineering*. Hoboken, NJ, USA: Wiley, 2016, pp. 1–42.
- [24] D. Goll, D. Schuller, G. Martinek, T. Kunert, J. Schurr, C. Sinz, T. Schubert, T. Bernthaler, H. Riegel, and G. Schneider, "Additive manufacturing of soft magnetic materials and components," *Additive Manuf.*, vol. 27, pp. 428–439, May 2019.
- [25] M. Garibaldi, I. Ashcroft, J. N. Lemke, M. Simonelli, and R. Hague, "Effect of annealing on the microstructure and magnetic properties of soft magnetic Fe-Si produced via laser additive manufacturing," *Scripta Mater.*, vol. 142, pp. 121–125, Jan. 2018.
- [26] J. Krishnasamy and M. Hosek, "Spray-formed hybrid-field traction motor," SAE Tech. Paper 0148–7191, 2017.
- [27] Z.-Y. Zhang, K. J. Jhong, C.-W. Cheng, P.-W. Huang, M.-C. Tsai, and W.-H. Lee, "Metal 3D printing of synchronous reluctance motor," in *Proc. IEEE Int. Conf. Ind. Technol. (ICIT)*, Mar. 2016, pp. 1125–1128.
- [28] A. D. Goodall, F. Nishanth, E. L. Severson, and I. Todd, "Loss performance of an additively manufactured axial flux machine stator with an eddy-current limiting structure," *Mater. Today Commun.*, vol. 35, Jun. 2023, Art. no. 105978.
- [29] M. Garibaldi, C. Gerada, I. Ashcroft, and R. Hague, "Free-form design of electrical machine rotor cores for production using additive manufacturing," *J. Mech. Design*, vol. 141, no. 7, Jul. 2019, Art. no. 071401.
- [30] B. Lizarribar, B. Prieto, M. Martínez-Iturralde, and G. Artetxe, "Novel topology optimization method for weight reduction in electrical machines," *IEEE Access*, vol. 10, pp. 67521–67531, 2022.
- [31] A. M. Ajamloo, A. Ghaheri, H. Shirzad, and E. Afjei, "Non-linear analytical modelling and optimisation of a 12/8 rotor excited flux-switching machine," *IET Electric Power Appl.*, vol. 14, no. 9, pp. 1592–1603, Sep. 2020.
- [32] K. A. Liogas, K. B. Lau, Z. Wang, D. N. Brown, E. Polatidis, P. Wang, and A. M. Korsunsky, "Effect of heat treatment on the microstructure and magnetic properties of laser powder bed fusion processed equiatomic Co-Fe," *Additive Manuf.*, vol. 67, Apr. 2023, Art. no. 103499.
- [33] L. Gargalis, "Optimisation of silicon content in Fe-Si alloys processed via laser powder bed fusion for an additively manufactured soft magnetic core," Dept. Mech., Mater. Manuf. Eng., Univ. Nottingham, Nottingham, U.K., Tech. Rep. 66013, 2021.
- [34] J. F. Gieras, *Permanent Magnet Motor Technology: Design and Applications*. Boca Raton, FL, USA: CRC Press, 2009.
- [35] A. Ghaheri, A. M. Ajamloo, H. Torkaman, and E. Afjei, "Design, modelling and optimisation of a slot-less axial flux permanent magnet generator for direct-drive wind turbine application," *IET Electr. Power Appl.*, vol. 14, no. 8, pp. 1327–1338, Aug. 2020.
- [36] J. Song, F. Dong, J. Zhao, H. Wang, Z. He, and L. Wang, "An efficient multiobjective design optimization method for a PMSLM based on an extreme learning machine," *IEEE Trans. Ind. Electron.*, vol. 66, no. 2, pp. 1001–1011, Feb. 2019.
- [37] A. D. Goodall, G. Yiannakou, L. Chechik, R. L. Mitchell, G. W. Jewell, and I. Todd, "Geometrical control of eddy currents in additively manufactured Fe-Si," *Mater. Design*, vol. 230, Jun. 2023, Art. no. 112002.

- [38] A. Manninen, J. Pippuri-Mäkeläinen, T. Riipinen, T. Lindroos, S. Metsä-Kortelainen, and A. Antikainen, "The mitigation of eddy-current losses in ferromagnetic samples produced by laser powder bed fusion," *IEEE Access*, vol. 10, pp. 115571–115582, 2022.
- [39] F. Mahmouditabar, A. Vahedi, and F. Marignetti, "The demagnetization phenomenon in PM machines; Principles, modelling, and design considerations," *IEEE Access*, vol. 11, pp. 47750–47773, 2023.
- [40] G. Bertotti, "General properties of power losses in soft ferromagnetic materials," *IEEE Trans. Magn.*, vol. MAG-24, no. 1, pp. 621–630, Jan. 1988.
- [41] S. Urbanek and B. Ponick, "Surface eddy current loss reduction in additively manufactured permanent magnet rotor active parts," in *Proc. 13th Int. Conf. Electr. Mach. (ICEM)*, Sep. 2018, pp. 1317–1322.
- [42] T. H. Group. *Cold Working Properties*. Accessed: Dec. 2023. [Online]. Available: <https://hghouston.com/cold-working>
- [43] J. S. Corp. *Electrical Steel Sheets*. Accessed: Dec. 2023. [Online]. Available: <https://www.jfe-steel.co.jp/en/products/electrical/catalog/f1e-001.pdf>



**AKBAR MOHAMMADI AJAMLOO** received the B.Sc. degree in electrical engineering and the M.Sc. degree in electrical machines and power electronics from the K. N. Toosi University of Technology, Tehran, Iran, in 2016 and 2018, respectively. He is currently pursuing the Ph.D. degree with the Department of Electromechanical, Systems and Metal Engineering, Ghent University, Gent, Belgium. His research interests include advanced topologies, multi-physics analysis, optimization, and analytical modeling of electrical machines. He is also deeply involved in the additive manufacturing of electromagnetic components for industrial and sustainable energy applications.



**MOHAMED N. IBRAHIM** (Senior Member, IEEE) received the M.Sc. degree in electrical power and machines engineering from Tanta University, Egypt, in November 2012, and the Ph.D. degree in electromechanical engineering from Ghent University, Belgium, in December 2017. He became a Teaching Assistant and an Assistant Professor (on leave) with the Electrical Engineering Department, Kafrelsheikh University, Egypt, in November 2008 and April 2018, respectively. Since December 2017, he has been a Postdoctoral Researcher with the Department of Electromechanical, Systems and Metal Engineering, Ghent University. Since August 2023, he has been an Associate Professor (on leave) with the Electrical Engineering Department, Kafrelsheikh University. He is currently an Affiliate Member of Flanders Make, the strategic research center for the manufacturing industry in Flanders, Belgium. He has over 100 publications and one patent in this research field. His research interests include electrical machines and drives for sustainability. He was a recipient of several times the Kafrelsheikh University Award for his international scientific publications. He serves as an Associate Editor for *IEEE TRANSACTIONS ON MAGNETICS* and as the Guest Editor for *Energies*, *Mathematics*, and *Electronics*. He is a Reviewer of several journals and conferences, including *IEEE TRANSACTIONS*.



**PETER SERGEANT** (Senior Member, IEEE) received the master's and Ph.D. degrees in electromechanical engineering from Ghent University, Ghent, Belgium, in 2001 and 2006, respectively. He became a Postdoctoral Researcher and an Associate Professor, in 2006 and 2012, respectively. Since 2022, he has been a Full Professor with Ghent University. His research interests include electrical machines and drives for industrial, automotive, and sustainable energy applications, with a focus on accurate modeling, prototyping and testing of machines and drives, for improving reliability, energy efficiency, and power density.

• • •